Editors' Suggestion

Coexistence of magnon and spinon excitations in $SeCuO_3$

Youngsu Choi,[1] Dirk Wulferding,[2,*] Kalaivanan Raju,[3] Raman Sankar,[3,†] and Kwang-Yong Choi[1,‡]
[1]*Department of Physics, Sungkyunkwan University, Suwon 16419, Republic of Korea*
[2]*Department of Physics and Astronomy, Sejong University, Seoul 05006, Republic of Korea*
[3]*Institute of Physics, Academia Sinica, Nankang, Taipei 11529, Taiwan*

(Received 8 April 2026; revised 26 June 2026; accepted 20 July 2026; published 6 August 2026)

Low-energy magnetic excitations are investigated in $SeCuO_3$ using temperature-, field-, and angle-dependent Raman scattering. We observe the coexistence of a sharp magnon mode and a broad spinon continuum, reflecting the interplay between long-range magnetic order and low-dimensional quantum fluctuations. Upon cooling, spectral weight is progressively transferred from the continuum to the magnon mode. In addition, both excitations exhibit an identical angular dependence governed by the same Raman scattering symmetry, indicating a common coupling to the underlying exchange geometry. Under an applied magnetic field, deviations from fourfold symmetry in the crossed polarization channel reveal the emergence of anisotropic spin correlations. These results suggest that coherent magnons develop from fractionalized spinon excitations in a low-dimensional quantum magnet.

DOI: 10.1103/87nc-z981

I. INTRODUCTION

Quantum spin systems composed of multiple magnetic sublattices, each with different spin topologies, dimensionalities, and competing interactions, provide a fertile platform for exploring exotic magnetic phases and an exceptionally rich spectrum of quasiparticle excitations. In such complex magnetic geometries, a hierarchy of energy scales naturally emerges: dominant exchange interactions dictate the high-energy excitations, while weaker residual couplings determine the magnetic ground state and shape the low-energy dynamics.

In conventional magnetic systems, a single dominant type of excitation typically reflects the underlying ground state. Concretely, long-range ordered magnets support magnons (collective spin-wave modes), whereas spin dimers or valence-bond solid systems host triplon excitations. In contrast, quantum spin liquids and one-dimensional antiferromagnetic chains exhibit fractionalized spinon excitations that form broad continua rather than sharp coherent modes [1–10]. These excitations are usually mutually exclusive as they stem from fundamentally different magnetic correlations.

However, this standard description is no longer valid in magnets with multiple inequivalent sublattices and competing interactions. In such systems, different sublattices with disparate local magnetic correlations enable the simultaneous occurrence of diverse quasiparticle excitations within a single material. A prototypical example is $SeCuO_3$ (space group $P2_1/n$) with two inequivalent Cu sites [11–17]. The Cu1 ions form strongly coupled dimers harboring triplon excitations, while the Cu2 ions form antiferromagnetic (AFM) spin chains featuring spinon continua. Similar phenomena have been observed in other systems. For instance, the layered copper hydroxides $Cu_2(OH)_3X$ ($X =$ halide, nitrate) realize chains of corner-sharing triangles with alternating AFM and ferromagnetic (FM) interactions [18–22]. By varying the inserted species X, one can tune the in-plane and interplane interactions to enable the coexistence of FM chains (magnons) and AFM chains (spinon continua). In the anisotropic triangular antiferromagnet $Ca_3ReO_5Cl_2$, exchange anisotropy and effective dimensional reduction lead to the simultaneous presence of one- and two-spinon continua alongside triplon excitations [23–28]. These examples highlight the importance of systematically exploring how quasiparticle excitations emerge, coexist, and evolve in complex magnetic systems.

In this work, we investigate the landscape of low-lying magnetic excitations in $SeCuO_3$ using inelastic light (Raman) scattering. The primary magnetic structure is built from tetramer units, in which a strong AFM exchange $J_1 = 270 - 308$ K couples the central Cu1–Cu1 dimer via edge-sharing CuO_4 plaquettes [11–17]. This dimer is further connected to Cu2 spins through a substantial coupling $J_2 \approx 160$ K. Weak intertetramer interactions give rise to quasi-one-dimensional tetramer chains along the a axis [upper panel of Fig. 1(a)]. In addition, alternating J_4–J_5 chains run along the a axis within the ab plane, which are coupled through J_3 interaction [see the lower panel of Fig. 1(a)]. Here, we note that the intrachain interaction of $J_4 \sim 39$ K is considerably weaker than the exchange interactions that define the tetramer units, resulting in a well-defined energy separation between high-energy tetramer excitations and low-energy spin-chain behavior. Residual couplings eventually stabilize the three-dimensional AFM order below the Néel temperature $T_N = 8$ K.

Our magnetic Raman scattering measurements reveal an excitation spectrum comprising a broad spinon continuum below 9 meV and a magnonlike mode below 4 meV. Notably,

*Contact author: d.wulferding@sejong.ac.kr
†Contact author: sankarndf@gmail.com
‡Contact author: choisky99@skku.edu

2469-9950/2026/114(7)/074407(10)

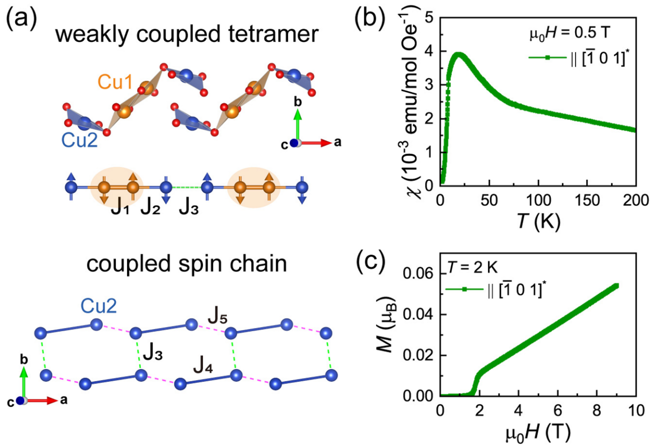

FIG. 1. (a) Magnetic structure of $SeCuO_3$. The top illustrates weakly coupled Cu1–Cu2 tetramers, where exchange interactions J_1 and J_2 define the intratetramer couplings and J_3 represents the intertetramer interaction. The bottom depicts an alternating J_4-J_5 spin-chain network within the *ab* plane. J_3 corresponds to the interchain coupling. (b) Temperature dependence of the magnetic susceptibility $\chi(T)$ measured under a magnetic field $\mu_0 H = 0.5$ T applied parallel to $[\bar{1}\,0\,1]^*$. (c) Field dependence of the magnetization $M(H)$ measured at $T = 2$ K for the same orientation.

both excitations exhibit an identical angular dependence of their scattering intensity, indicating that the magnon mode results from the confinement of spinons.

II. EXPERIMENTAL DETAILS

Polycrystalline $SeCuO_3$ was synthesized via a conventional solid-state reaction method. Stoichiometric amounts of CuO and SeO_2 powders ($3CuO : 3SeO_2$) were thoroughly mixed and ground using an agate mortar to ensure homogeneity. The mixture was placed in an alumina crucible, sealed in an evacuated quartz tube under a vacuum of approximately 10^{-2} Torr, and heated in a box furnace at 400 °C. To obtain a phase-pure product, the grinding and heating processes were repeated twice under the same conditions.

The resulting phase-pure $SeCuO_3$ powder was subsequently used as a precursor for single-crystal growth via the chemical vapor transport (CVT) method. The powder, together with $SeCl_4$ as the transport agent, was sealed in an evacuated quartz tube under a vacuum of approximately 10^{-2} Torr. The sealed quartz ampoule was then placed in a two-zone furnace. Crystal growth was carried out under a temperature gradient, with the source zone maintained at 610 °C and the growth zone at 540 °C. The system was kept under these conditions for two weeks to enable efficient transport and growth of $SeCuO_3$ single crystals.

To confirm the sample quality, we performed magnetic susceptibility measurements. The temperature dependence of the magnetic susceptibility $\chi(T)$, shown in Fig. 1(b), exhibits a broad hump around 100 K, followed by a pronounced maximum near 19 K, and a rapid decrease toward zero at lower temperatures. This behavior is consistent with the development of short-range spin correlations within the tetramer units and along the effective spin chains. The strong suppression of $\chi(T)$ at low temperatures indicates the magnetic easy axis along the $[\bar{1}\,0\,1]^*$ direction, which is further supported by the spin-flop-like transition observed in the magnetization at $T = 2$ K [see Fig. 1(c)]. Notably, the small spin-flop field, $\mu_0 H_{sf} \approx 1.8$ T, alludes to the weak Ising anisotropy and therefore implies a magnon gap that is much smaller than the dominant exchange energy scale [16]. Overall, our $\chi(T)$ and $M(H)$ data are in good agreement with earlier reports.

Polarization- and temperature-dependent low frequency (8–500 cm^{-1}) Raman spectra were recorded using a 561 nm laser (Oxxius) focused onto the sample surface with a spot diameter of about 50 micrometers and a laser power below $P = 1.5$ mW. The sample was mounted into a closed-cycle magneto-optical cryostat (Oxford SpectroMag PT). Raman-scattered signals were dispersed through a Princeton Instruments TriVista777 spectrometer onto a PyLoN eXcelon CCD detector. Raman spectra were acquired from the crystallographic *ab* plane, with both the incident and scattered light polarizations lying within the *ab* plane. For the field-dependent Raman measurements, the magnetic field was applied approximately along the crystallographic *c* axis.

III. RESULTS AND DISCUSSION

To map out the landscape of low-lying excitations, we performed temperature- and angle-dependent Raman scattering measurements. We did not observe triplon excitations expected in the range of $\hbar\omega = 30$–35 meV, possibly due to their overlap with highly intense phonon modes. In the following, we focus on magnetic excitations originating from the spin-chain subsystems. A detailed discussion of the phonon modes is provided in the Appendix.

Figure 2(a) presents the temperature evolution of the Raman response in $SeCuO_3$, measured in parallel polarization within the *ab* plane (see Fig. 5 for the full spectral range). The low-energy spectra reveal two distinct magnetic features: a sharp *M* mode at 3.65 meV and a broad continuum *S* extending up to 9 meV. We assign the sharp *M* mode to a magnon-related collective excitation, inferred from its sharp linewidth, its emergence in the magnetically ordered phase, and its energy scale, which closely matches the maximum of the magnon dispersion (~4 meV) reported by inelastic neutron scattering (INS) [16]. Although one-magnon Raman scattering is generally weak in collinear antiferromagnets, anisotropic exchange interactions, such as Dzyaloshinskii-Moriya terms, are known to enable a finite one-magnon Raman intensity [29]. Similar one-magnon Raman signals have been reported in related Cu-based antiferromagnets [22,30].

As an alternative assignment, a two-magnon interpretation appears unlikely because the observed mode is relatively sharp, whereas two-magnon excitations typically manifest as broad spectral features due to the large phase space of two-particle states. Likewise, a crystal-field origin is improbable because Cu^{2+} ions possess a largely quenched orbital degree of freedom, and crystal-field excitations are generally expected at substantially higher energies. Nonetheless, given the small energy scale associated with the spin-flop field [see Fig. 1(c)], the *M* peak cannot be treated simply as a conventional transverse magnon. Instead, its energy closely

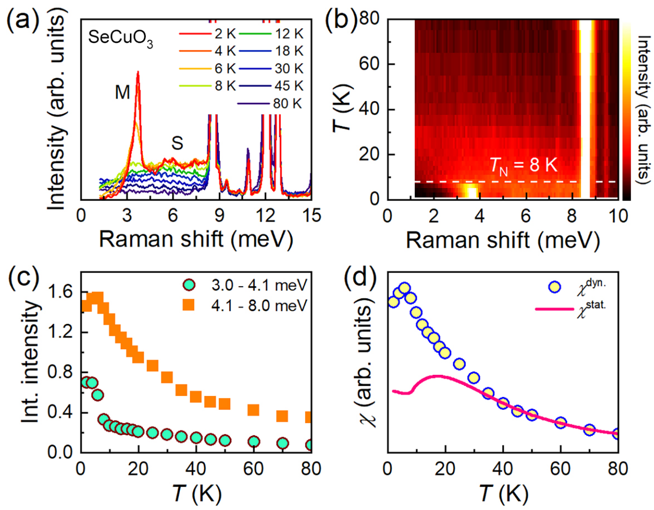

FIG. 2. (a) Temperature-dependent Raman spectra of $SeCuO_3$, focusing on low-energy magnetic excitations. The peak labeled M corresponds to a magnon mode, while S denotes a spinon continuum. (b) Color map of the Raman intensity as a function of temperature and Raman shift. The dashed horizontal line marks the Néel temperature $T_N \approx 8$ K. (c) Temperature dependence of the integrated Raman intensity in two energy windows, $\hbar\omega = 3.0$–4.1 meV and 4.1–8.0 meV. (d) Comparison between the dynamic susceptibility χ^{dyn}, extracted from the Raman response, and the static magnetic susceptibility χ^{stat} obtained from bulk magnetization measurements.

matches the maximum of the magnon dispersion (∼4 meV) [16]. Taken together, these observations suggest that a simple transverse-magnon picture is insufficient. We therefore cannot exclude a more complex collective magnetic response, in particular a longitudinal magnon mode, which can arise in weakly coupled spin-chain systems due to interchain coupling.

The thermal evolution of the magnetic Raman response is further illustrated by the false-color intensity map in Fig. 2(b). In contrast to the sharp M mode, which emerges only in the magnetically ordered phase, a broad low-energy continuum is already present well above T_N. The continuum intensity increases upon cooling below approximately 50 K and reaches a maximum near the broad peak in the magnetic susceptibility around 19 K, indicating its close connection to the development of short-range spin-spin correlations. Upon entering the magnetically ordered phase, the continuum becomes partially gapped and weakly structured, while the sharp M mode emerges at an energy close to the gap scale. This suggests a redistribution of spectral weight from a broad continuum in the paramagnetic regime to a more well-defined collective excitation in the ordered state.

In weakly coupled spin-chain systems, a broad magnetic continuum can often be interpreted either as multimagnon excitations or as confined fractionalized spinons. Notably, an INS study revealed that the magnetic continuum observed above the single-magnon band at energies around 4 meV favors a spinon-excitation scenario [16]. Within this spinon-confinement framework, the magnonlike mode at 3.65 meV can be understood as a bound state formed below the spinon continuum. We recall that exchange-mediated magnetic Raman scattering can create pairs of spinon excitations with opposite momenta and thus samples a momentum-integrated magnetic response weighted by the Raman form factor [33].

Specifically, for one-dimensional $S = 1/2$ Heisenberg antiferromagnets, Raman scattering probes two-spinon continua with intensity $I(\omega) \propto \sum_k f_k \delta(\omega - 2\omega_i(k))$, bounded by the des Cloizeaux-Pearson dispersions $\omega_1(k) = \pi J/2|\sin(k)|$ and $\omega_2(k) = \pi J|\sin(k/2)|$. Here, f_k is a filtering factor that restricts Raman contributions to a high-energy cutoff at $E_h = 2\omega_1(k = \pi/2) = \pi J$ [31,32]. Using the observed high-energy cutoff of approximately 9 meV, we estimate the dominant intrachain exchange interaction as $J \sim 2.86$ meV ($\cong 33$ K), which is comparable to $J_4 \sim 39$ K.

To quantify these trends, we integrate the Raman intensity $I_{int}(T)$ over two energy ranges: I_{int}^{low} in the lower-energy range ($\hbar\omega = 3.0$–4.1 meV) and I_{int}^{high} in the higher-energy window ($\hbar\omega = 4.1$–8.0 meV). As compared in Fig. 2(c), $I_{int}^{low}(T)$ exhibits a steeper increase than $I_{int}^{high}(T)$ with decreasing temperature through T_N, suggesting that the spinon excitations become less confined above the one-magnon energy scale. We further estimate the dynamic Raman susceptibility from the Bose-factor-corrected Raman response, $I(\omega, T) \propto [1 + n(\omega, T)]\chi''(\omega, T)$, as

$$\chi^{dyn}(T) \sim \int_{1\ \mathrm{meV}}^{10\ \mathrm{meV}} \frac{\chi''(\omega, T)}{\omega} d\omega. \tag{1}$$

Here, the integration range corresponds to the magnetic-excitation window displayed in Fig. 2(b). Compared to $\chi^{stat}(T)$, $\chi^{dyn}(T)$ shows a pronounced enhancement below 30 K [see circles in Fig. 2(d)]. This discrepancy arises because the Raman-derived dynamic susceptibility selectively probes spin fluctuations associated with the spin-chain subsystem, whereas the uniform static susceptibility also includes contributions from tetramer singlets, which suppress the overall magnetic response.

To gain further insight into the nature of the magnetic excitations, we investigated their angular dependence. Before analyzing the angular dependence, the strong phonon mode near 8.6 meV was fitted by a Gaussian lineshape and subtracted from the raw spectra shown in Fig. 2(a) and Fig. 5. Figure 3(a) shows the resulting magnetic Raman spectra at selected rotation angles θ and at $T = 2$ K. The angle θ is measured with respect to the a axis within the ab plane. As evident from the color and polar plots of Figs. 3(b) and 3(c), both the magnon mode M and the spinon excitation S display a pronounced twofold symmetry in the (xx) scattering geometry. In the crossed (xy) polarization, the angular variation of the Raman spectra and the corresponding intensity map reveal a characteristic fourfold pattern for the spinon and magnon excitations [see Figs. 3(d)–3(f)]. This correspondence indicates that both excitations share the same symmetry character, possibly due to their common microscopic origins. Such behavior further suggests that the underlying Raman coupling mechanism is governed by the same symmetry-allowed scattering channel.

Within the Loudon-Fleury framework, the magnetic Raman operator is given by [34,35]

$$\mathcal{R} = \sum_{\langle i,j\rangle} (\mathbf{e}_{in} \cdot \hat{r}_{ij})(\mathbf{e}_{out} \cdot \hat{r}_{ij})\mathbf{S}_i \cdot \mathbf{S}_j, \tag{2}$$

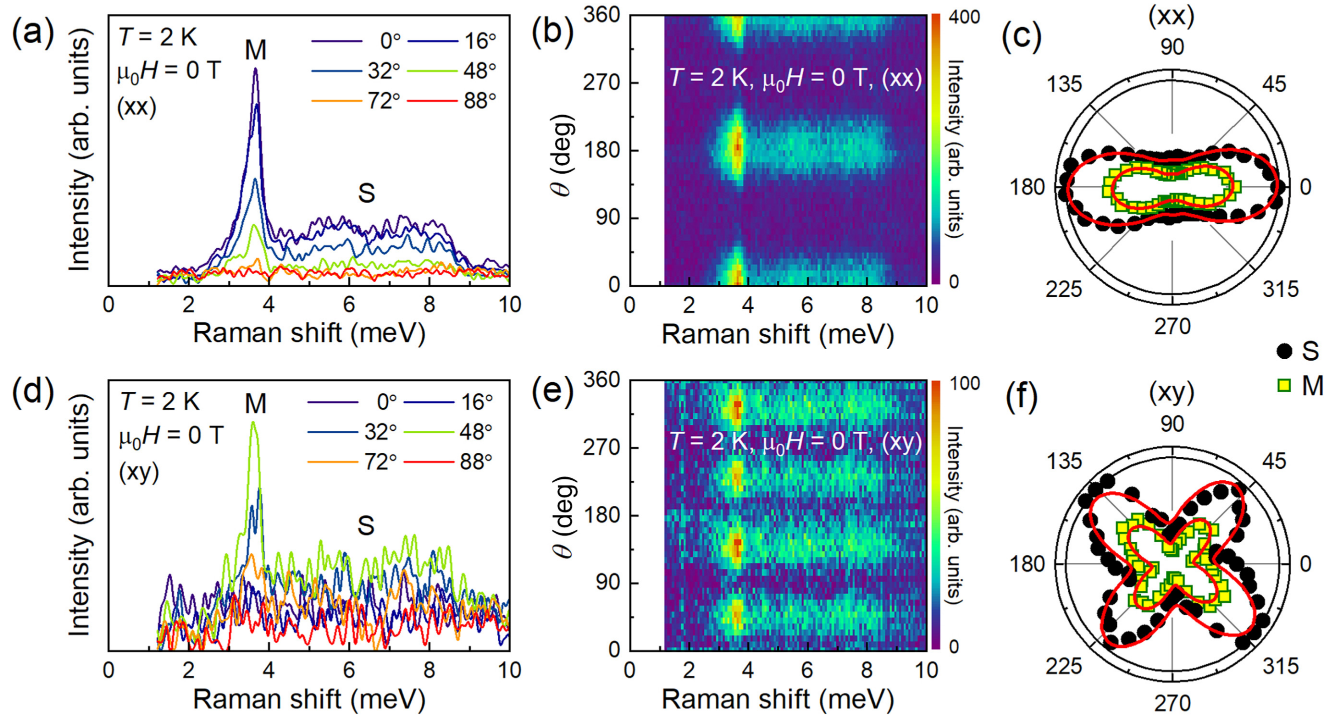

FIG. 3. Angle-dependent Raman response of $SeCuO_3$ measured at $T = 2$ K and $\mu_0 H = 0$ T. (a) Magnetic Raman spectra measured in the parallel (xx) polarization configuration at rotation angles θ within the ab plane. The peak labeled M corresponds to a magnon excitation, while S denotes a spinon continuum. (b) Color map of the Raman intensity in the (xx) configuration as a function of θ and Raman shift. (c) Polar plots of the normalized Raman intensities for the spinon (S; black circles) and magnon (M; yellow squares) excitations in the (xx) configuration. Solid lines are fits as described in the main text. (d) Raman spectra measured in the crossed (xy) polarization for different θ. (e) Corresponding false-color map of the Raman intensity in the (xy) configuration. (f) Polar plots of the normalized Raman intensities for S and M, together with fits based on the Loudon-Fleury theory.

where $\mathbf{e}_{\text{in}}$ and $\mathbf{e}_{\text{out}}$ are the polarization vectors of the incident and scattered light, and $\hat{r}_{ij}$ is the unit vector connecting the sites i and j. For parallel polarization, we take $\mathbf{e}_{\text{in}} = \mathbf{e}_{\text{out}} = (\cos\theta, \sin\theta)$. Considering an alternating chain along the a axis and interchain coupling along the b axis [see the bottom of Fig. 1(a)], the Raman operator is expressed as

$$\mathcal{R}_{xx}(\theta) = (\mathbf{e}\cdot\hat{x})^2 \sum_i \mathbf{S}_{i,j}\cdot\mathbf{S}_{i+1,j} + (\mathbf{e}\cdot\hat{y})^2 \sum_j \mathbf{S}_{i,j}\cdot\mathbf{S}_{i,j+1} \propto a\cos^2\theta + b\sin^2\theta, \tag{3}$$

where the constants a and b parametrize the intrachain and interchain contributions, respectively. In the crossed polarization with $\mathbf{e}_{\text{in}} = (\cos\theta, \sin\theta)$ and $\mathbf{e}_{\text{out}} = (-\sin\theta, \cos\theta)$, we obtain

$$\mathcal{R}_{xy}(\theta) \propto (-a+b)\cos\theta\sin\theta. \tag{4}$$

The magnetic Raman intensity $I(\theta,\omega) \propto \langle \mathcal{R}(t)\mathcal{R}(0)\rangle_\omega$ can thus be written as

$$I_{xx}(\theta,\omega) = [a\cos^2\theta + b\sin^2\theta]^2 S(\omega), \tag{5}$$

$$I_{xy}(\theta,\omega) = (a-b)^2\cos^2\theta\sin^2\theta\, S(\omega), \tag{6}$$

where $S(\omega) = \sum_{i,j}\langle(\mathbf{S}_i\cdot\mathbf{S}_{i+1})(t)(\mathbf{S}_j\cdot\mathbf{S}_{j+1})(0)\rangle$ denotes the spin-spin correlation function. At zero magnetic field, assuming isotropic correlations, $I(\theta,\omega)$ becomes independent of $S(\omega)$, yielding purely geometric intensity variations. We note that the angular dependence of the magnetic Raman intensities in the parallel and crossed polarization transforms according to the A_g and B_g Raman tensors, respectively.

For the polar plots in Figs. 3(c) and 3(f), a constant offset c was included to account for the residual background. In the parallel channel, the data were fitted by

$$I_{xx}(\theta) = [a\cos^2\theta + b\sin^2\theta]^2 + c. \tag{7}$$

The best fits yielded $b = 0$, with $(a, c) = (0.662, 0.125)$ for the M mode and $(0.849, 0.257)$ for the S continuum. In the crossed channel,

$$I_{xy}(\theta) = (a-b)^2\cos^2\theta\sin^2\theta + c, \tag{8}$$

giving $(a-b, c) = (0.645, 0.060)$ for the M mode and $(0.854, 0.127)$ for the S excitation.

Figures 4(a) and 4(d) exhibit the angular dependence of the magnetic Raman spectra at $\mu_0 H = 7$ T and $T = 2$ K. In the (xx) configuration, the angular patterns remain essentially unchanged compared to the zero-field case. At 7 T, the parallel-channel data were fitted using the same form, yielding $b = 0$, with $(a, c) = (0.721, 0.104)$ for M and $(0.890, 0.201)$ for S. In sharp contrast, the (xy) polarization spectra show deviations from the simple fourfold symmetry. The finite-field Raman response can be decomposed into a zero-field-like fourfold term and an additional field-induced twofold contribution,

$$I_{xy}(\theta, B) = a^2\sin^2(2\theta) + b^2\cos^2(\theta-\theta_0). \tag{9}$$

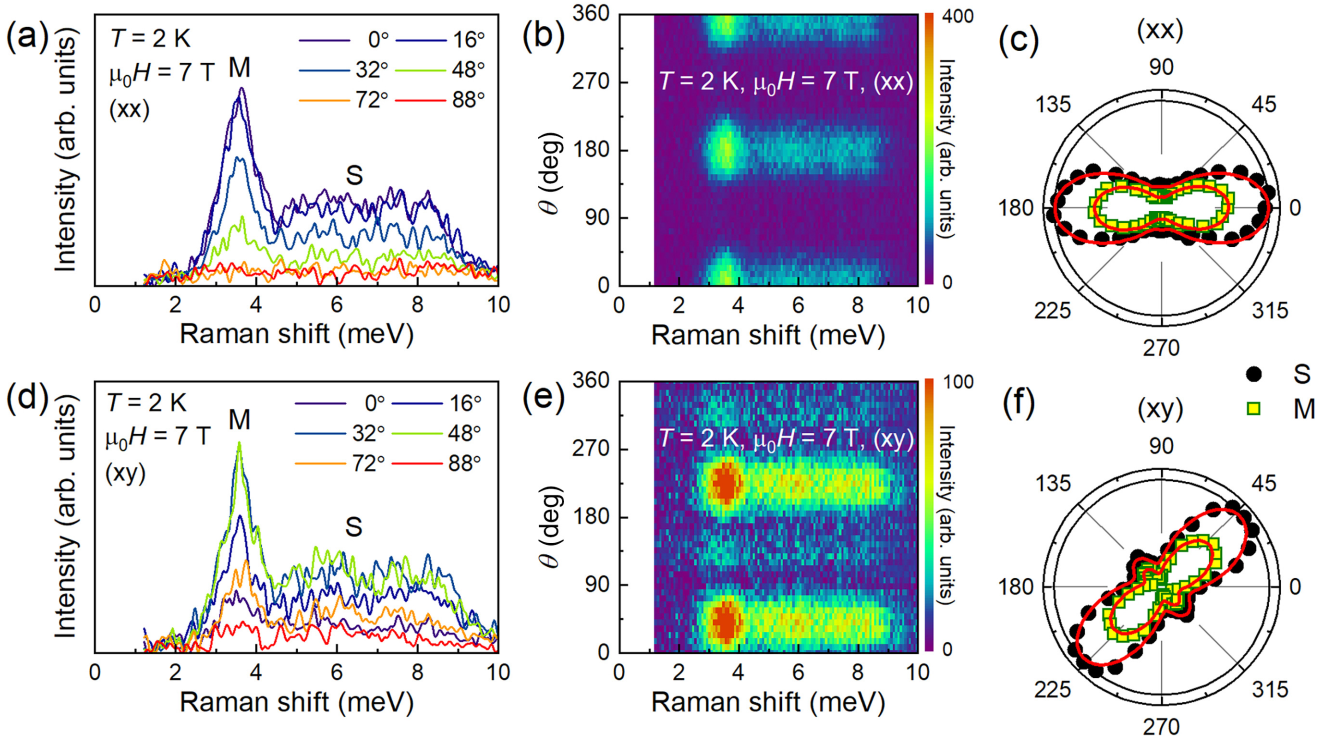

FIG. 4. Angular variation of the magnetic Raman spectra measured at $T = 2$ K under an applied magnetic field $\mu_0 H = 7$ T. (a) Magnetic Raman spectra measured in the (xx) polarization configuration. The M peak corresponds to a magnon excitation, while S denotes a spinon continuum. (b) Color map of the Raman intensity in the (xx) configuration as a function of θ and Raman shift. (c) Polar plots of the normalized Raman intensity for the spinon (S) and magnon (M) contributions in the (xx) configuration. Solid lines are fits based on the Loudon-Fleury framework. (d) Raman spectra measured in the (xy) polarization configuration at different rotation angles θ. (e) Corresponding color map of the magnetic Raman intensity. (f) Polar plots of the normalized Raman intensity for the spinon (S) and magnon (M) contributions in the (xy) configuration, together with theoretical fits.

Fits yield $(a, b, \theta_0) \approx (0.370, 0.495, 42.6^\circ)$ for the magnon mode and $(0.469, 0.644, 42.7^\circ)$ for the spinon continuum. Notably, both excitations exhibit a similar offset angle of approximately 42°. Since the B_g phonons are not affected by the applied magnetic field, this behavior should not be attributed to a field-dependent modulation of the Raman tensor [see Fig. 7(d) in the Appendix]. Rather, this behavior is associated with the development of anisotropic spin correlations in the presence of a magnetic field. In general, an applied field induces a finite magnetization, $\langle \mathbf{S}^z \rangle \neq 0$, leading to a disparity between longitudinal and transverse spin correlations. As a result, the field breaks spin-rotational symmetry, allowing additional symmetry components, such as a twofold term $\cos^2\theta$. In contrast to the crossed polarization, the parallel (xx) configuration predominantly probes bond-aligned fluctuations, where the light polarization couples to a chain direction. Consequently, there is no mixing between orthogonal components, and no additional angular harmonics are generated.

Finally, we address the identical angular dependence observed for the magnon mode and the spinon continuum. Since one-magnon and two-magnon (or multispinon) Raman processes originate from fundamentally different scattering mechanisms, there is *a priori* no requirement that they share the same angular dependence dictated by the underlying exchange geometry. We recall that first-order Raman scattering processes predominantly probe excitations near $q \approx 0$, whereas higher-order Raman processes involving two-magnon or multiparticle spinon excitations effectively probe an integral over the Brillouin zone, weighted by the corresponding two-particle (or multiparticle) density of states. Consequently, the observed angular dependence reflects the symmetry of the effective Raman vertex rather than a specific excitation momentum. Within a scenario in which the 3.65 meV magnon mode is interpreted as a bound state emerging from the spinon continuum, the similar angular dependence of the two responses can be naturally understood. In this case, the bound-state nature of the excitation may also account for its relatively sharp, resonancelike Raman response. Consistent with this picture, Figs. 2(a) and 2(b) show that, as the magnon becomes thermally destabilized, its spectral weight is gradually transferred to the spinon continuum without the formation of incoherent paramagnon excitations (pronounced quasielastic scattering) at elevated temperatures.

IV. CONCLUSION

In summary, our temperature-, field-, and angle-dependent Raman scattering study of $SeCuO_3$ enables mapping out the landscape of low-energy magnetic excitations. We observe the coexistence of a sharp magnon mode at low energies and a broad spinon continuum at higher energies, highlighting the dual character of magnetic excitations in this quasi-one-dimensional system. The extracted energy scale of the continuum is consistent with the dominant intrachain exchange interaction, supporting the presence of an effective spin-chain subsystem, which is energetically well separated from a tetramer subsystem.

The identical angular dependence of the magnon and spinon excitations demonstrates that both couple to the same symmetry-allowed Raman channel, governed by the underlying exchange geometry. This common symmetry is compatible with a confined-spinon scenario or, alternatively, with a longitudinal magnon excitation associated with the ordered phase, although Raman data alone cannot distinguish unambiguously between these possibilities. Furthermore, the field-induced symmetry breaking observed in the crossed polarization channel reveals the development of anisotropic spin correlations, while the parallel channel remains symmetry protected. These results establish $SeCuO_3$ as a promising platform for exploring the crossover between fractionalized and coherent magnetic excitations in low-dimensional quantum magnets.

ACKNOWLEDGMENTS

The work at SKKU was supported by the National Research Foundation (NRF) of Korea (Grants No. RS-2023-00209121 and No. 2020R1A5A1016518). R.S. acknowledges the financial support provided by the Ministry of Science and Technology in Taiwan under Projects No. 115-2124-M-001-004 and No. NSTC-113-2112M001-045-MY3, as well as support from Academia Sinica for the budget of ASiMATE-115-14. Y.C. acknowledges the support from the NRF of Korea (Grant No. RS-2023-00214312). D.W. acknowledges support from the Institute of Applied Physics of Seoul National University, from the ITRC Program through the IITP, and from the Global Research Development Center (GRDC) Cooperative Hub Program through the NRF, funded by the (MSIT) (Grants No. RS-2024-00437191 and No. RS-2023-00258359).

DATA AVAILABILITY

The data that support the findings of this article are not publicly available. The data are available from the authors upon reasonable request.

APPENDIX A: TEMPERATURE DEPENDENCE OF RAMAN SPECTRA AND PHONON MODES IN $SeCuO_3$

Figure 5(a) presents the as-measured zero-field spectra, allowing the evolution of both the magnetic continuum and phonon modes to be tracked up to 80 K. The background intensity level is indicated by dashed black lines for reference. As the temperature increases above T_N, the gapped and weakly structured continuum extending up to 10 meV becomes featureless and the gap closes. With further increase in temperature, spectral weight is continuously transferred toward lower energies, leading to a quasielastic response characteristic of thermally driven spin fluctuations. At the highest measured temperature (80 K, corresponding to approximately 10 T_N), the low-energy magnetic signal is largely suppressed and merges with the background within our experimental sensitivity.

Figure 5(b) shows the temperature-dependent Raman spectra over a broader energy range, where several intense phonon modes are clearly observed. To examine the temperature evolution of the lattice response, we analyzed selected phonon modes at 8.6, 30.8, and 56.3 meV. The extracted phonon frequency, full width at half maximum (FWHM), and normalized intensity are summarized in Fig. 5(c).

The temperature dependence of the phonon frequency and linewidth was fitted using a conventional anharmonic phonon model [36],

$$\omega(T) = \omega_0 - A\left[1 + \frac{2}{\exp\left(\frac{\hbar\omega_0}{2k_B T}\right) - 1}\right], \tag{A1}$$

and

$$\Gamma(T) = \Gamma_0 + B\left[1 + \frac{2}{\exp\left(\frac{\hbar\omega_0}{2k_B T}\right) - 1}\right], \tag{A2}$$

where ω_0 and Γ_0 are the zero-temperature phonon frequency and linewidth, respectively, and A and B describe the strength of anharmonic phonon decay.

As shown by the solid black lines in Fig. 5(c), the overall temperature evolution of the phonon frequencies and linewidths is largely captured by the anharmonic model. However, small deviations from the anharmonic behavior become visible below approximately 35 K, particularly in the phonon frequency and linewidth. This temperature scale is well above T_N and is close to the regime where short-range magnetic correlations develop. Therefore, the deviations may reflect a weak coupling between the phonon response and short-range spin correlations. In contrast, no abrupt phonon anomaly is observed at T_N, indicating that the onset of long-range magnetic order does not induce a sizable lattice distortion detectable in the Raman phonon response.

APPENDIX B: ANGULAR DEPENDENCE OF PHONON MODES IN $SeCuO_3$

To determine the symmetry of the phonon excitations in $SeCuO_3$, we performed angle-dependent polarized Raman measurements. The crystal belongs to the monoclinic space group $P2_1/n$ (No. 14), whose corresponding point group is C_{2h}. According to the factor-group analysis, the Raman-active phonon modes are classified into A_g and B_g symmetries.

Within the semiclassical description, the Raman scattering intensity is given by [34]

$$I \propto |\mathbf{e}_{\text{in}} \cdot R \cdot \mathbf{e}_{\text{out}}|^2, \tag{B1}$$

where $\mathbf{e}_{\text{in}}$ and $\mathbf{e}_{\text{out}}$ are the polarization vectors of the incident and scattered light, and R is the Raman tensor. In an absorptive medium, the tensor elements generally acquire complex phases [34,37]. The Raman tensors for the A_g and B_g modes

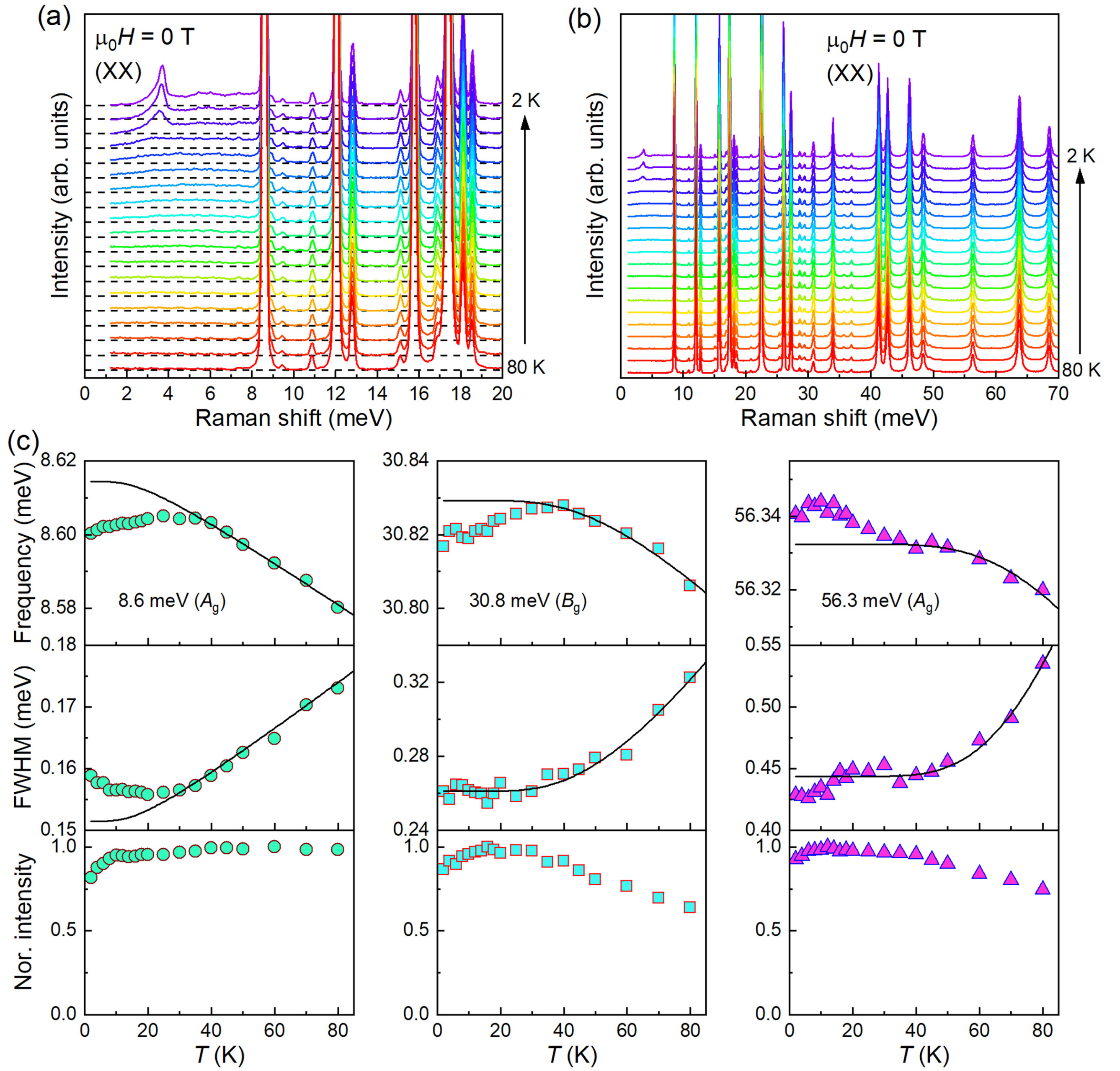

FIG. 5. (a) Low-energy spectral range measured at $\mu_0 H = 0$ T in the (xx) configuration. Individual spectra are vertically shifted for clarity, and the dashed black lines mark the background for each spectrum. (b) Raman spectra over a broad spectral range measured under the same conditions, showing intense phonon modes. (c) Temperature dependence of the frequency, full width at half maximum (FWHM), and normalized intensity of selected phonon modes. Solid black lines denote fits to an anharmonic phonon model.

are thus written as

$$R(A_g) = \begin{pmatrix} |a|e^{i\phi_a} & 0 & |d|e^{i\phi_d} \\ 0 & |b|e^{i\phi_b} & 0 \\ |d|e^{i\phi_d} & 0 & |c|e^{i\phi_c} \end{pmatrix}, \tag{B2}$$

$$R(B_g) = \begin{pmatrix} 0 & |e|e^{i\phi_e} & 0 \\ |e|e^{i\phi_e} & 0 & |f|e^{i\phi_f} \\ 0 & |f|e^{i\phi_f} & 0 \end{pmatrix}. \tag{B3}$$

In our experimental geometry, the incident and scattered light polarizations lie within the ab plane, and the angle θ is measured with respect to the a axis. The Raman intensities in the parallel (xx) and crossed (xy) configurations are given by

$$I_{A_g}^{XX}(\theta) = [a\cos^2\theta\cos\phi + b\sin^2\theta]^2 + a^2\cos^4\theta\sin^2\phi, \tag{B4}$$

$$I_{B_g}^{XX}(\theta) = e^2\ \sin^2(2\theta), \tag{B5}$$

$$I_{A_g}^{XY}(\theta) = [(a - b\cos\phi)^2 + b^2\sin^2\phi]\cos^2\theta\sin^2\theta, \tag{B6}$$

$$I_{B_g}^{XY}(\theta) = e^2\ \cos^2(2\theta), \tag{B7}$$

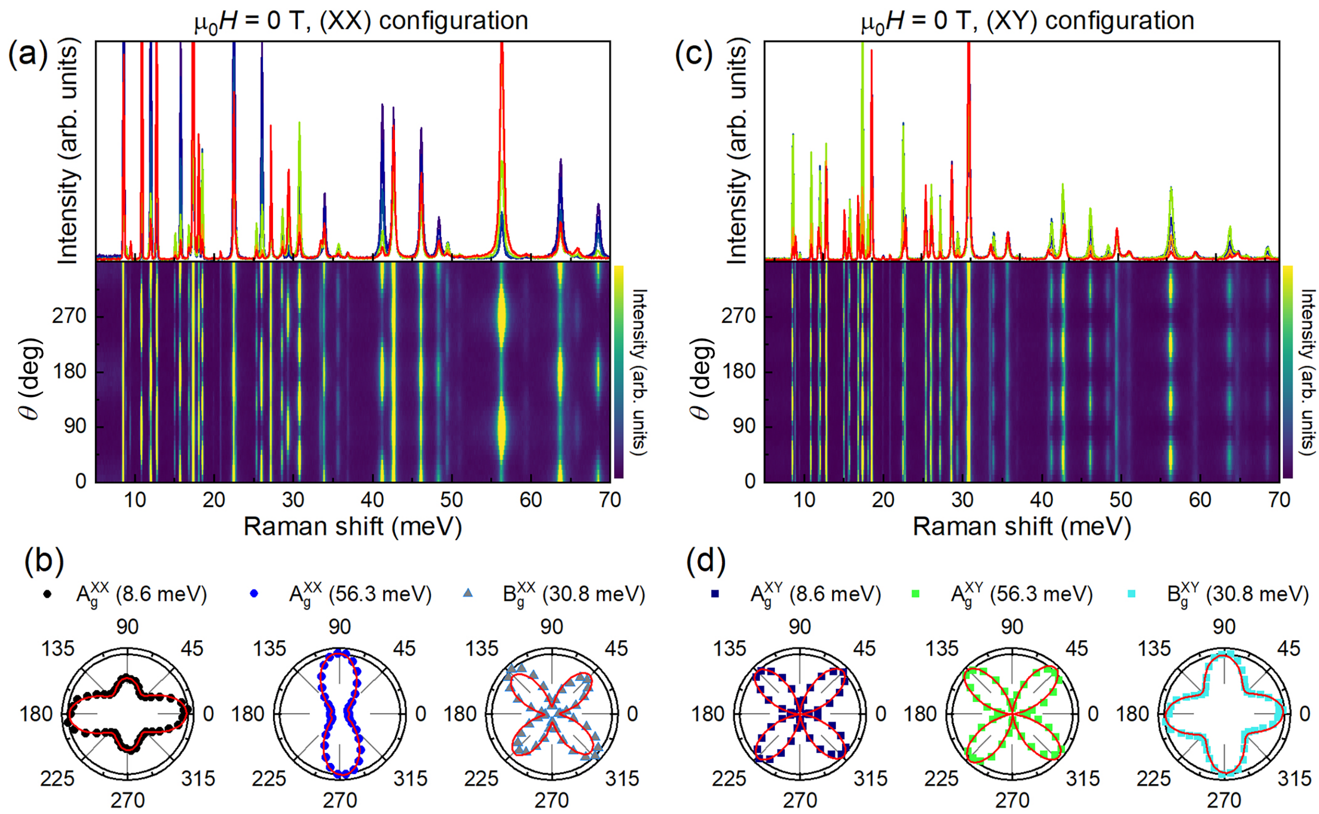

FIG. 6. Polarization- and angle-dependent Raman response of $SeCuO_3$ at $\mu_0H = 0$ T used for phonon symmetry analysis. (a) Raman spectra (upper) and corresponding color map (lower) as a function of rotation angle θ in the (xx) polarization configuration. (b) Polar plots of the normalized Raman intensity for selected phonon modes A_g (8.6 meV), A_g (56.3 meV), and B_g (30.8 meV) in the (xx) configuration. Symbols represent experimental data and solid lines are fits based on the Raman tensors. (c) Raman spectra (upper) and corresponding color map (lower) in the (xy) polarization configuration. (d) Polar plots of the normalized Raman intensity for the same phonon modes in the (xy) configuration, together with Raman tensor fits.

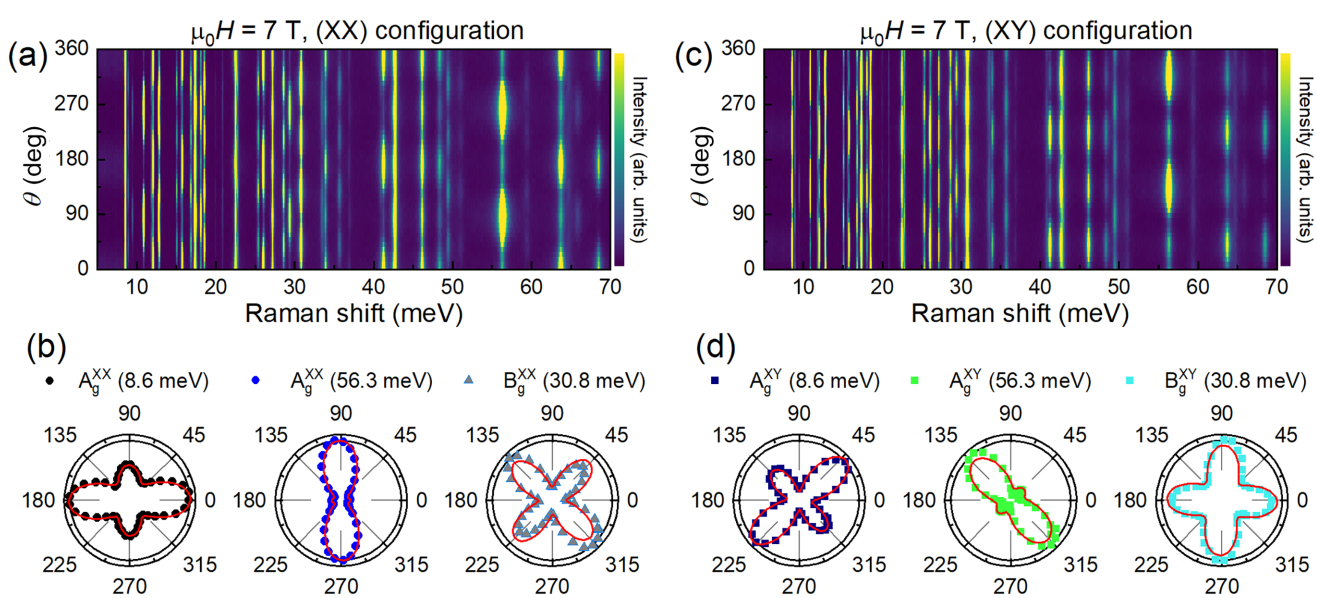

FIG. 7. Polarization- and angle-dependent Raman response of $SeCuO_3$ at $\mu_0H = 7$ T. (a) Color map of the Raman intensity as a function of rotation angle θ and Raman shift in the (xx) polarization configuration. (b) Polar plots of the normalized Raman intensity for selected phonon modes A_g (8.6 meV), A_g (56.3 meV), and B_g (30.8 meV) in the (xx) configuration. Symbols represent experimental data and solid lines are fits based on the Raman tensors. (c) Color map of the Raman intensity in the (xy) polarization configuration. (d) Polar plots of the normalized Raman intensity for the same phonon modes in the (xy) configuration, together with Raman tensor fits.

where $\phi = \phi_a - \phi_b$ is the relative phase between the tensor elements.

Figure 6 shows the angle-dependent Raman spectra measured at $\mu_0 H = 0$ T. The observed angular patterns are well reproduced by the above expressions. In the (xx) configuration, the extracted parameters for the A_g modes are $(a, b) \approx (0.987, 0.774)$ for the 8.6 meV mode and (0.393, 1.00) for the 56.3 meV mode, with phase differences $\phi \approx 85.2^\circ$ and 83.8°, respectively. The B_g mode at 30.8 meV follows the expected angular dependences, with $e \approx 0.88$ in the (xx) geometry and $e \approx 0.68$ in the (xy) geometry.

Figure 7 presents the corresponding measurements under an applied magnetic field of $\mu_0 H = 7$ T. In the (xx) configuration, the parameters for the A_g modes remain nearly unchanged compared to the zero-field case, with $(a, b) \approx (1.005, 0.769)$ and (0.395, 0.998), and phase differences $\phi \approx 93.9^\circ$ and 96.9° for the 8.6 meV and 56.3 meV modes, respectively. The B_g mode also retains its characteristic angular dependence.

In contrast, a pronounced modification is observed for the A_g modes in the (xy) configuration. The angular profiles deviate significantly from the zero-field $\sin^2\theta\cos^2\theta$ form and cannot be described by the same expression. Instead, the data are well captured by an empirical form,

$$I_{A_g}^{XY}(\theta) = a^2 \sin^2(2\theta) + b^2 \cos^2(\theta - \theta_0), \tag{B8}$$

which introduces an additional anisotropic contribution beyond the zero-field symmetry constraints. The fitted parameters are $(a, b, \theta_0) \approx (0.810, 0.611, 39.9^\circ)$ for the 8.6 meV mode and $(0.539, 0.777, 42.9^\circ)$ for the 56.3 meV mode.

These results demonstrate that the magnetic field selectively modifies the A_g symmetry channel, primarily affecting the crossed polarization response, while leaving the (xx) configuration and the B_g modes largely unchanged.

[1] D. I. Khomskii, *Basic Aspects of the Quantum Theory of Solids: Order and Elementary Excitations* (Cambridge University Press, Cambridge, 2010).

[2] H. Bethe, Zur Theorie der Metalle. I. Eigenwerte und Eigenfunktionen der linearen Atomkette, Z. Phys. **71**, 205 (1931).

[3] L. D. Faddeev and L. A. Takhtajan, What is the spin of a spin wave? Phys. Lett. A **85**, 375 (1981).

[4] J. des Cloizeaux and J. J. Pearson, Spin-wave spectrum of the antiferromagnetic linear chain, Phys. Rev. **128**, 2131 (1962).

[5] T. Kulka, M. Panfil, M. Berciu, and K. Wohlfeld, Nature of spinons in 1D spin chains, Phys. Rev. Lett. **134**, 236504 (2025).

[6] P. Lemmens, K.-Y. Choi, E. E. Kaul, C. Geibel, K. Becker, W. Brenig, R. Valentí, C. Gros, M. Johnsson, P. Millet, and F. Mila, Evidence for an unconventional magnetic instability in the spin-tetrahedra system $Cu_2Te_2O_5Br_2$, Phys. Rev. Lett. **87**, 227201 (2001).

[7] K. Y. Choi, J. W. Hwang, P. Lemmens, D. Wulferding, G. J. Shu, and F. C. Chou, Evidence for dimer crystal melting in the frustrated spin-ladder system $BiCu_2PO_6$, Phys. Rev. Lett. **110**, 117204 (2013).

[8] K.-Y. Choi, S. Do, P. Lemmens, J. van Tol, J. Shin, G. S. Jeon, Y. Skourski, J.-S. Rhyee, and H. Berger, Coexistence of localized and collective magnetism in the coupled-spin-tetrahedra system $Cu_4Te_5O_{12}Cl_4$, Phys. Rev. B **90**, 184402 (2014).

[9] P. McClarty, F. Krüger, T. Guidi, S. F. Parker, K. Refson, A. W. Parker, D. Prabhakaran, and R. Coldea, Topological triplon modes and bound states in a Shastry–Sutherland magnet, Nat. Phys. **13**, 736 (2017).

[10] D. Wulferding, Y. Choi, S. Lee, M. A. Prosnikov, Y. Gallais, P. Lemmens, C. Zhong, H. Kageyama, and K.-Y. Choi, Thermally populated versus field-induced triplon bound states in the Shastry-Sutherland lattice $SrCu_2(BO_3)_2$, npj Quantum Mater. **6**, 102 (2021).

[11] I. Živković, D. M. Djokić, M. Herak, D. Pajić, K. Prša, P. Pattison, D. Dominko, Z. Mickovi'c, D. Cinćić, L. Forró, H. Berger, and H. M. Rønnow, Site-selective quantum correlations revealed by magnetic anisotropy in the tetramer system $SeCuO_3$, Phys. Rev. B **86**, 054405 (2012).

[12] M. Herak, A. G. Čabo, D. Žilić, B. Rakvin, K. Salamon, O. Milat, and H. Berger, Magnetic anisotropy of the spin tetramer system $SeCuO_3$ studied by torque magnetometry and ESR spectroscopy, Phys. Rev. B **89**, 184411 (2014).

[13] S. Lee, W.-J. Lee, J. van Tol, P. L. Kuhns, A. P. Reyes, H. Berger, and K.-Y. Choi, Anomalous spin dynamics in the coupled spin tetramer system $CuSeO_3$, Phys. Rev. B **95**, 054405 (2017).

[14] T. Cvitanić, V. Surija, K. Prša, O. Zaharko, I. Kupčić, P. Babkevich, M. Frontzek, M. Požek, H. Berger, A. Magrez, H. M. Rønnow, M. S. Grbić, and I. Zivković, Singlet state formation and its impact on the magnetic structure in the tetramer system $SeCuO_3$, Phys. Rev. B **98**, 054409 (2018).

[15] N. Novosel, W. Lafargue-Dit-Hauret, Z. Rapljenović, M. Dragičević, H. Berger, D. Cinčić, X. Rocquefelte, and M. Herak, Strong decoupling between magnetic subsystems in the low-dimensional spin-1/2 antiferromagnet $SeCuO_3$, Phys. Rev. B **99**, 014434 (2019).

[16] L. Testa, V. Surija, K. Prsa, P. Steffens, M. Boehm, P. Bourges, H. Berger, B. Normand, H. M. Rønnow, and I. Zivkovic, Triplons, magnons, and spinons in a single quantum spin system: SeCuO3, Phys. Rev. B **103**, L020409 (2021).

[17] X. Rocquefelte, M. Herak, A. Miyake, W. Lafargue-Dit-Hauret, H. Berger, M. Tokunaga, and A. Saúl, Coherent description of the magnetic properties of $SeCuO_3$ versus temperature and magnetic field, Phys. Rev. B **107**, 054407 (2023).

[18] H. Zhang, Z. Zhao, D. Gautreau, M. Raczkowski, A. Saha, V. O. Garlea, H. Cao, T. Hong, H. O. Jeschke, S. D. Mahanti, T. Birol, F. F. Assaad, and X. Ke, Coexistence and interaction of spinons and magnons in an antiferromagnet with alternating antiferromagnetic and ferromagnetic quantum spin chains, Phys. Rev. Lett. **125**, 037204 (2020).

[19] L. Heinze, H. O. Jeschke, I. I. Mazin, A. Metavitsiadis, M. Reehuis, R. Feyerherm, J.-U. Hoffmann, M. Bartkowiak, O. Prokhnenko, A. U. B. Wolter, X. Ding, V. S. Zapf,

C. Corvalan Moya, F. Weickert, M. Jaime, K. C. Rule, D. Menzel, R. Valenti, W. Brenig, and S. Süllow, Magnetization process of atacamite: A case of weakly coupled $S = 1/2$ sawtooth chains, Phys. Rev. Lett. **126**, 207201 (2021).

[20] D. M. Gautreau, A. Saha, and T. Birol, First principles characterization of the magnetic properties of $Cu_2(OH)_3Br$, Phys. Rev. Mater. **5**, 024407 (2021).

[21] L. Heinze, T. Kotte, R. Rausch, A. Demuer, S. Luther, R. Feyerherm, E. L. Q. N. Ammerlaan, U. Zeitler, D. I. Gorbunov, M. Uhlarz, K. C. Rule, A. U. B. Wolter, H. Kühne, J. Wosnitza, C. Karrasch, and S. Süllow, Atacamite $Cu_2Cl(OH)_3$ in high magnetic fields: Quantum criticality and dimensional reduction of a sawtooth-chain compound, Phys. Rev. Lett. **134**, 216701 (2025).

[22] D. Wulferding, S. S. Islam, Y. Choi, G. Ban, S. Lee, A. Pawbake, C. Faugeras, K.-Y. Choi, Field- and temperature-driven magnetic excitations in rouaite $Cu_2(OH)_3NO_3$, Phys. Rev. B **111**, 064409 (2025).

[23] D. Hirai, T. Yajima, D. Nishio-Hamane, C. Kim, H. Akiyama, M. Kawamura, T. Misawa, N. Abe, T. Arima, and Z. Hiroi, Visible 5d orbital states in a pleochroic oxychloride, J. Am. Chem. Soc. **139**, 10784 (2017).

[24] D. Hirai, K. Nawa, M. Kawamura, T. Misawa, and Z. Hiroi, One-dimensionalization by geometrical frustration in the anisotropic triangular lattice of the $5d$ quantum antiferromagnet $Ca_3ReO_5Cl_2$, J. Phys. Soc. Jpn. **88**, 044708 (2019).

[25] K. Nawa, D. Hirai, M. Kofu, K. Nakajima, R. Murasaki, S. Kogane, M. Kimata, H. Nojiri, Z. Hiroi, and T. J. Sato, Bound spinon excitations in the spin-1/2 anisotropic triangular antiferromagnet $Ca_3ReO_5Cl_2$, Phys. Rev. Res. **2**, 043121 (2020)

[26] Y. Choi, S. H. Lee, J.-H. Lee, S. Y. Lee, M.-J. Seong, and K.-Y. Choi, Bosonic spinons in anisotropic triangular antiferromagnets, Nat. Commun. **12**, 6453 (2021).

[27] S. A. Zvyagin, A. N. Ponomaryov, J. Wosnitza, D. Hirai, Z. Hiroi, M. Gen, Y. Kohama, A. Matsuo, Y. H. Matsuda, and K. Kindo, Dimensional reduction and incommensurate dynamic correlations in the triangular-lattice antiferromagnet $Ca_3ReO_5Cl_2$, Nat. Commun. **13**, 6310 (2022).

[28] M. Gen, D. Hirai, K. Morita, K. Nawa, S. Kogane, N. Matsuyama, T. Yajima, M. Kawamura, K. Deguchi, A. Koda, M. Kofu, S. Ohira-Kawamura, T. J. Sato, A. Matsuo, K. Kindo, Y. Kohama, and Z. Hiroi, Chemically tunable quantum magnetism on the anisotropic triangular lattice in rhenium oxyhalides, Nat. Commun. **16**, 9938 (2025).

[29] M. B. Silva Neto and L. Benfatto, One-magnon Raman scattering in La_2CuO_4: The origin of the field-induced mode, Phys. Rev. B **72**, 140401(R) (2005).

[30] S. Jeon, D. Wulferding, Y. Choi, S. Lee, K. Nam, K. H. Kim, M. Lee, T.-H. Jang, J.-H. Park, S. Lee, S. Choi, C. Lee, H. Nojiri, and K.-Y. Choi, One-ninth magnetization plateau stabilized by spin entanglement in a kagome antiferromagnet, Nat. Phys. **20**, 435 (2024).

[31] D. Wulferding, Y. Choi, W. Lee, and K.-Y. Choi, Raman spectroscopic diagnostic of quantum spin liquids, J. Phys.: Condens. Matter **32**, 043001 (2020).

[32] K.-Y. Choi, W.-J. Lee, A. Glamazda, P. Lemmens, D. Wulferding, Y. Sekio, and T. Kimura, Competing lattice fluctuations and magnetic excitations in CuO, Phys. Rev. B **87**, 184407 (2013).

[33] P. H. M. van Loosdrecht, J. P. Boucher, G. Martinez, G. Dhalenne, and A. Revcolevschi, Inelastic light scattering from magnetic fluctuations in $CuGeO_3$, Phys. Rev. Lett. **76**, 311 (1996).

[34] R. Loudon, The Raman effect in crystals, Adv. Phys. **13**, 423 (1964).

[35] P. A. Fleury and R. Loudon, Scattering of light by one- and two-magnon excitations, Phys. Rev. **166**, 514 (1968).

[36] M. Balkanski, R. F. Wallis, and E. Haro, Anharmonic effects in light scattering due to optical phonons in silicon, Phys. Rev. B **28**, 1928 (1983).

[37] M. Cardona, *Light scattering in solids II* (Springer-Verlag Berlin, Heidelberg New York, 1982), Chap. 2, Vol. 50, pp. 19–278.